SCIENCE CHINA
Earth Sciences

•RESEARCH PAPER•

December 2022 Vol.65 No.12: 2267–2284
https://doi.org/10.1007/s11430-021-9963-8

Carbonate dynamics in a tropical coastal system in the South China Sea featuring upwelling, river plumes and submarine groundwater discharge

Wei YANG, Xianghui GUO, Zhimian CAO, Jianzhong SU, Liguo GUO, Lifang WANG, Yi XU, Tao HUANG, Yan LI, Yanping XU, Zhe WANG, Guizhi WANG & Minhan DAI*

State Key Laboratory of Marine Environmental Science, College of Ocean and Earth Sciences, Xiamen University, Xiamen 361102, China

Received April 19, 2021; revised June 4, 2022; accepted June 13, 2022; published online October 21, 2022

Abstract This study examined carbonate dynamics in the northwestern South China Sea (NWSCS), an area jointly influenced by upwelling, river plumes and submarine groundwater discharge. Data were obtained from two cruises conducted in summer 2009 and 2012. In 2009, a high salinity-low temperature water mass occurred nearshore off northeastern Hainan Island, indicative of upwelling, commonly referred to as HNEU. A river plume fueled primarily by local rivers and characterized by low salinity and high temperature was observed in the NWSCS off the mainland roughly along the 30 m isobath. In 2012, coastal upwelling off northeastern Hainan Island was not detectable at the surface, but was observed at a different location off eastern Hainan Island (HEU). River plume waters in 2012 were patchily distributed, with a low salinity zone further westerly than that in 2009 and another on the mid-shelf of the NWSCS sourced from the Pearl River which reached out ~250 km from the mouth of the Pearl River Estuary. In 2009, elevated dissolved inorganic carbon (DIC) and total alkalinity (TA) occurred in the coastal plume, where submarine groundwater discharge contributed DIC and TA additions of 38.9±20.5 and 42.5±22.3 μmol kg^{-1}, respectively, with a DIC/TA ratio of ~0.92, which made a minor contribution to the variation of seawater partial pressure of CO_2 (pCO_2), pH and the aragonite saturation state index (Ω_{arag}). Additionally, high surface phytoplankton production consumed DIC of 10.0±10.4 μmol kg^{-1} but did not significantly affect TA, which dominated pCO_2 drawdown in the coastal plume water and increased the pH and Ω_{arag} at surface. Submarine groundwater discharge was also observed in the region influenced by upwelling, but to a lesser degree than that impacted by coastal plume. Lower pH and Ω_{arag} and higher pCO_2 values than in offshore waters were observed downstream of the upwelling system, attributable largely to organic matter remineralization with a DIC addition of 23.8±8.4 μmol kg^{-1}. In 2012, submarine groundwater discharge was not detected but high phytoplankton production dominated carbonate dynamics in the coastal plume water with a net DIC consumption of 104.2 μmol kg^{-1}, which markedly drew down sea surface pCO_2 and increased pH and Ω_{arag}. In the Pearl River Plume, the solubility-driven CO_2 sink exceeded biological CO_2 uptake, resulting in an additional decrease of pH and Ω_{arag} and increase of seawater pCO_2. Taken together, this study demonstrated complex spatial and year-to-year variability, and the controls of the carbonate system under the joint modulations of upwelling, river plumes and submarine groundwater discharge. A first order estimate that considered the rise of atmospheric CO_2 and seawater temperature further suggested a high risk of ocean acidification in this coastal area by the end of this century, which could be amplified under the stresses of river plumes, submarine groundwater discharge and organic matter remineralization.

Keywords Carbonate system, Northwestern South China Sea, Coastal upwelling, Submarine groundwater discharge, Ocean acidification

Citation: Yang W, Guo X, Cao Z, Su J, Guo L, Wang L, Xu Y, Huang T, Li Y, Xu Y, Wang Z, Wang G, Dai M. 2022. Carbonate dynamics in a tropical coastal system in the South China Sea featuring upwelling, river plumes and submarine groundwater discharge. Science China Earth Sciences, 65(12): 2267–2284, https://doi.org/10.1007/s11430-021-9963-8

* Corresponding author (email: mdai@xmu.edu.cn)

© Science China Press and Springer-Verlag GmbH Germany, part of Springer Nature 2022

https://engine.scichina.com/doi/10.1007/s11430-021-9963-8

1. Introduction

Upwelling is a ubiquitous coastal ocean feature (e.g., Friederich et al., 2002; Torres, 2003; Cao et al., 2011; Xue et al., 2016). Stimulated by upwelled nutrients, biological primary production in upwelling zones is typically high and sustains high fisheries production (e.g., Risien et al., 2004; Barth et al., 2007; Jing et al., 2011; Xue et al., 2016). How upwelling impacts the ocean carbonate system and air-sea carbon dioxide (CO_2) flux has been a subject of considerable interest (e.g., Feely et al., 2008; Huang et al., 2015; Xu et al., 2016), although it remains controversial. In many upwelling systems with a high upwelling intensity, such as the central California and northern Chile systems (Friederich et al., 2002; Torres, 2003), the increase in primary productivity stimulated by nutrients cannot compensate for the free CO_2 brought up from depth, resulting in its release from the ocean (Torres, 2003; Santana-Casiano et al., 2009; Cai, 2011; Cao et al., 2011; Xue et al., 2016). However, in some upwelling systems, the higher nutrient supply and subsequent biological consumption of dissolved inorganic carbon (DIC) lead to strong net CO_2 uptake. These systems include the northern California upwelling system off Oregon, the upwelling system off the Galician coast, the Benguela upwelling system, and the western Canada upwelling system (e.g., Borges and Frankignoulle, 2002; Hales et al., 2005; Santana-Casiano et al., 2009; Evans et al., 2012; Cao et al., 2014). The CO_2 flux pattern varies temporally over different evolution stages and/or spatially in different upwelling subzones even within a single system (e.g., Hales et al., 2005; Cao et al., 2014). In the Oregon coastal upwelling, it is initiated by a strong CO_2 source due to outcropping of CO_2-enriched subsurface water to the very nearshore zone over short timescales. This upwelled water is then transported seaward and southward and partial pressure of CO_2 (pCO_2) is drawn down by biological productivity to ~200 μatm (1 atm=1.01325×10^5 Pa), far below the atmospheric pCO_2 value (Feely et al., 2008).

Upwelling not only brings up water with high CO_2 concentrations, but also lower pH and aragonite saturation state index (Ω_{arag}), which makes upwelling systems prone to ocean acidification (e.g., Feely et al., 2008, 2012; Lui et al., 2015; Xue et al., 2016). The dynamics of pH and Ω_{arag}, however exhibit strong spatio-temporal variations and are subject to complex physical and biogeochemical controls within the water column (Cao et al., 2011; Xue et al., 2016). At the air-sea interface, CO_2 degassing (source) reduces seawater pCO_2 but augments pH and Ω_{arag}. In contrast, CO_2 uptake (sink) increases seawater pCO_2 but reduces pH and Ω_{arag} (Xu et al., 2016; Xue et al., 2017). Moreover, these effects are often closely associated with local water circulation and the supply of source materials. For instance, river plumes alter wind-driven upwelling circulation by changing water column buoyancy and density structure (Gan et al., 2009; Dai et al., 2014), while submarine groundwater discharge contributes substantial material fluxes to the water column, which may enhance coastal acidification (e.g., Wang et al., 2014). Breakdown and quantification of the relative contributions from upwelling, river plumes and submarine groundwater discharge to carbonate dynamics in the coastal ocean are challenging and thus rarely reported (Gu et al., 2012; Luo et al., 2017; Dai et al., 2021).

The South China Sea is the largest marginal sea of the North Pacific Ocean (Dai et al., 2013 and references therein). On its northern shelf, two prominent coastal upwelling systems have been previously reviewed by Hu and Wang (2016). One is the Eastern Guangdong upwelling along the coast between the cities Shanwei and Shantou (e.g., Cao et al., 2011; Gan et al., 2009, 2010; Han et al., 2012). The other occurs off Hainan Island in the northwestern South China Sea (NWSCS) (e.g., Lü et al., 2008; Lin et al., 2016a, 2016b; Dong et al., 2017), which is modulated by the upwelling-favorable wind, flow-topography interaction, and Ekman pumping (e.g., Jing et al., 2011, 2015; Hu and Wang, 2016; Lin et al., 2016a, 2016b; Xie et al., 2017).

Our study area is located in the NWSCS featuring upwelling off Hainan Island, where coral reefs are widely distributed (Wang et al., 2014; Dong et al., 2017). Dong et al. (2017) examined the influence of coastal upwelling on a fringing reef system on the eastern coast of Hainan Island, and indicated that upwelled waters with low pH and Ω_{arag} pose a high ocean acidification risk to this nearshore coral reef system. Wang et al. (2014) suggested that submarine groundwater discharge is another important contributor to acidification in a coastal coral reef system in Sanya Bay, located southeast of Hainan Island. However, there has been thus far no quantitative assessment of carbonate dynamics in the NWSCS that considers upwelling, river plumes and submarine groundwater discharge. Lack of this knowledge hampers our ability to assess the current status and predict future directions of the marine ecosystem, especially coral reefs that are of great societal concern.

This study investigates the carbonate system in the NWSCS using data collected during two summer cruises in 2009 and 2012. The changes in DIC and total alkalinity (TA) and subsequently the ocean acidification attributed to different water masses/processes were quantified, and the potential risks of ocean acidification to the marine ecosystem were predicted in the context of global climate change.

2. Materials and methods

2.1 Study area

Modulated primarily by the Asian monsoon, the NWSCS in summer is influenced by river plumes from the Pearl River and local rivers, as well as coastal upwelling (Hu and Wang,

https://engine.scichina.com/doi/10.1007/s11430-021-9963-8

2016; Lin et al., 2016a, 2016b; Dong et al., 2017). The Pearl River is the second largest river in China in terms of freshwater discharge with an annual runoff of 3.26×10^{11} m^3, of which ~80% takes place during the wet season between April and October (Dai et al., 2014; Guo and Wong, 2015). The Pearl River Plume on the northern shelf of the South China Sea is a prominent feature in summer, which may extend southeastward up to a few hundred kilometers from the mouth of the estuary (e.g., Gan et al., 2009, 2010; Han et al., 2012; Yang et al., 2021; Zhao et al., 2021). Prior studies also suggest that the Pearl River Plume trajectory can be highly variable depending on wind stress and coastal currents. Coastal rivers, such as the Jianjiang River originating from the mainland, and the Wanquan and Wenchang Rivers from Hainan Island, may also influence the study area, but their discharges account for <2% of the Pearl River discharge (Lin et al., 2016b; Dong et al., 2017). Due to these very small discharges from coastal rivers, coastal plume waters were only observed nearshore (Lin et al., 2016b; Dong et al., 2017).

Coastal upwelling in the NWSCS typically starts in April, peaks from mid-July to mid-August, and disappears in September; in most cases it lasts 1–2 weeks (Hu and Wang, 2016). Upwelling in the NWSCS has been observed off the eastern coast of Hainan Island between the coasts of the cities of Wenchang and Wanning (so-called HEU), and off the northeastern coast of Hainan Island between the cities of Zhanjiang and Haikou (referred to as HNEU) (Lin et al., 2016b; Dong et al., 2017).

The submarine groundwater discharge is a particularly prominent feature at the highly permeable sediment-water interface, contributing abundant dissolved solutes to the water column (Gu et al., 2012; Liu et al., 2012, 2014; Luo et al., 2017; Tan et al., 2018). On the northern South China Sea shelf, surface sediments show a grain size gradation from gravel inshore to silt offshore, which consists of terrigenous and biogenous detritus, as well as authigenic minerals (Zhang et al., 2003; Liu et al., 2012). Results from radium isotopes (^{226}Ra and ^{228}Ra) estimated the submarine groundwater discharge on the northern South China Sea shelf to be 2.2×10^8–3.7×10^8 m^3 d^{-1}, equivalent to 12–21% of the Pearl River discharge. In turn, the DIC flux via submarine groundwater discharge was estimated to be 153×10^9–347×10^9 mol yr^{-1}, or equivalent to ~23–53% of the riverine DIC export flux (Liu et al., 2012). Recently, Dai et al. (2021) further confirmed the substantial contribution of submarine groundwater discharge to the DIC and TA in the NWSCS. In both studies, the DIC/TA ratio of the submarine groundwater discharge end-member varied in the range of ~0.9–1.1, which was however much lower than that in the Sanya Bay of ~3.3 (Wang et al., 2014). The different DIC/TA ratios of submarine groundwater discharge end-member suggested their spatial variability, and the need to better understanding of the influence of submarine groundwater discharge on the carbonate dynamics in the NWSCS.

2.2 Sampling and analysis

Sampling was conducted onboard the *R/V Dongfanghong II* in 2009 (Jul. 17–Aug. 16) and 2012 (Jul. 29–Aug. 21) in NWSCS (Figure 1). At each sampling station, temperature, salinity and depth were recorded with a Seabird® SBE 911 or 917 Conductivity-Temperature-Depth (CTD) sensor package. The distributions of temperature (T), salinity (S) and the T-S diagram during these two cruises were published in Lin et al. (2016a, 2016b) and Meng et al. (2017). During both cruises, water samples were collected at different depths throughout the water column with 30 L Go-Flo or 12 L Niskin bottles mounted on a rosette sampling assembly.

Samples for dissolved oxygen (DO), DIC and TA were taken with Tygon® tubing free of air bubbles, with ample sample overflow to minimize any contamination from atmospheric oxygen or CO_2. Samples for DO were collected with 60 mL biological oxygen demand bottles and fixed with Winkler reagents (Carpenter, 1965). Both DIC and TA samples were poisoned with $HgCl_2$-saturated solution upon sample collection; DIC samples were measured on shipboard within 24 h of sampling, and TA samples were stored in the dark and returned to a land-based laboratory for analysis within two months of collection. Samples for soluble reactive phosphorus (SRP or phosphate) measurements were filtered with 0.45 μm polyacetate filters and stored in 120 mL high-density polyethylene bottles and analyzed onboard within 24 h.

The DIC was measured by collecting and quantifying the CO_2 released from the sample upon acidification with a non-dispersive infrared detector (NDIR, Li-Cor® 7000), with a measurement precision better than ±0.1%; TA was determined by potentiometric Gran titration with a precision of ±2.0 μmol kg^{-1} (Cai et al., 2004). Measurements of DIC and TA were detailed in Cai et al. (2004). The accuracy of DIC and TA measurements was determined by calibration against certified reference materials provided by A. G. Dickson, Scripps Institution of Oceanography, U.S.A to an accuracy of better than ±2.0 μmol kg^{-1}. Seawater pH, Ω_{arag} and influences of processes on pCO_2 were calculated from measured DIC and TA using the CO2SYS program (Pierrot et al., 2006), in which the dissociation constants for carbonic acid were obtained from Mehrbach et al. (1973), as refitted by Dickson and Millero (1987), and the dissociation constant for HSO_4^- was determined as per Dickson (1990). The relationship of total boron with salinity followed Uppstrom (1967).

During the cruises, surface water was continuously pumped into analytical instruments from a side intake at a depth of ~5 m. Temperature and conductivity were measured

https://engine.scichina.com/doi/10.1007/s11430-021-9963-8

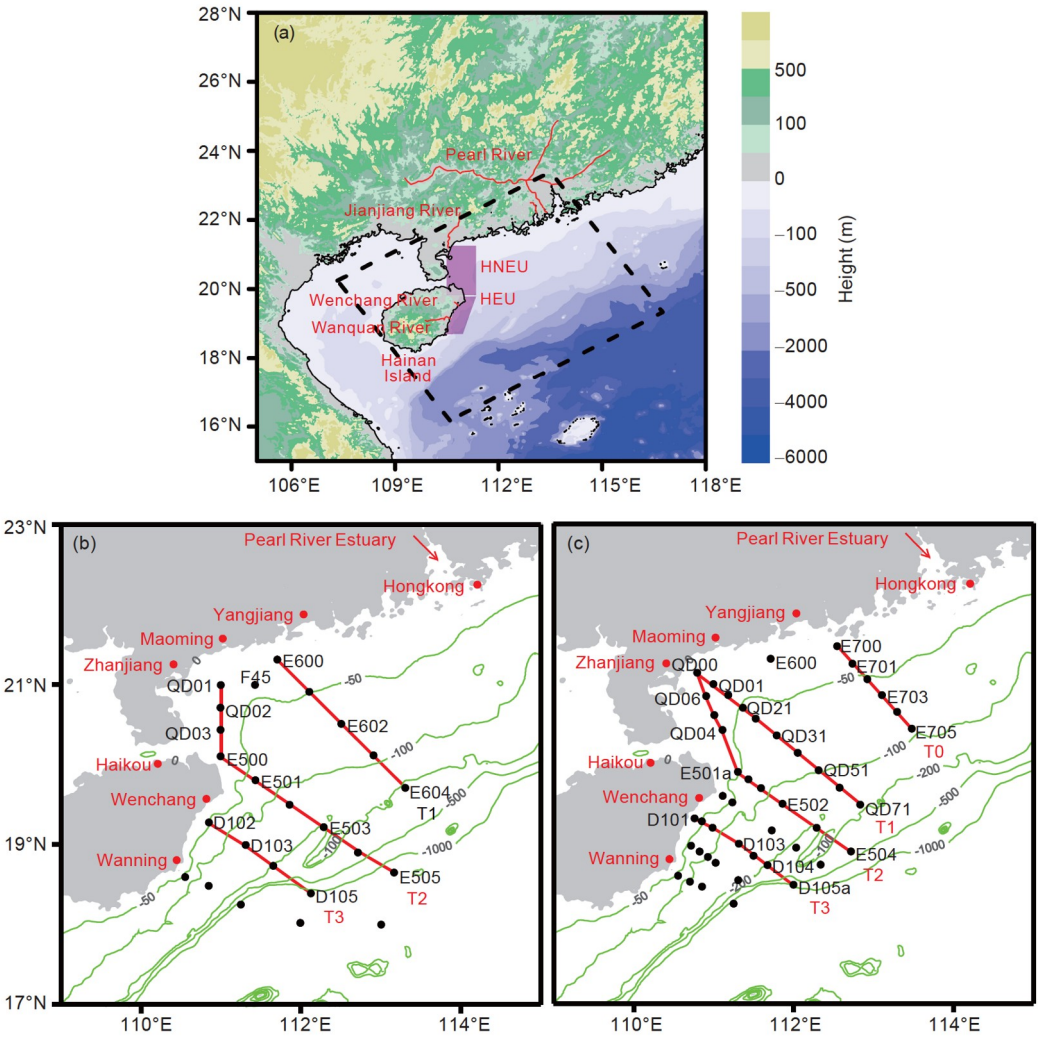

Figure 1 Maps showing the study area (a) and location of sampling stations during two summer cruises on July 17–Aug. 16, 2009 (b) and July 29–Aug. 21, 2012 (c) in the northwestern South China Sea (NWSCS). Also shown are the upwelling systems off the northeastern coast of Hainan Island (HNEU) in 2009 and off the eastern coast of Hainan Island (HEU) in 2012, following the description in Lin et al. (2016b). Vertical distributions of parameters measured along transects (T0 to T3) marked in red in panels (b) and (c) are detailed in the text. The Pearl River in southern China, the Jianjiang River in Leizhou Peninsula, and the Wanquan and Wenchang Rivers in Hainan Island are also shown.

continuously using an Idronaut Multiparameter "Flow Through" CTD recorder. A continuous-flow underway system with a cylinder-type equilibrator filled with plastic balls was used for air-sea equilibration (Zhai et al., 2005a, 2005b). The CO_2 mole fraction in dry air (xCO_2) was measured continuously using a Li-Cor® 7000 NDIR detector, which was calibrated against a series of CO_2 gas standards. The overall uncertainty of the xCO_2 measurements and pCO_2 data processing was <1% (Zhai et al., 2005a, 2013). Air pCO_2 was determined every 4–12 h, and the bow intake from which atmospheric air was pumped was installed ~6–10 m above the water surface to avoid ship contamination. The pCO_2 data used in this study have been published in Li et al. (2020).

DO samples were measured spectrophotometrically at 466 nm onboard within 4 h of sampling (Labasque et al., 2004). Samples were placed in a constant temperature bath at 25.0±0.1°C for at least 1 h before measurement. Soluble reactive phosphorus was determined with the phosphomolybdenum blue method (Du et al., 2013) and run with an AA3 Auto-Analyzer (Bran-Lube, GmbH). The detection limit was 0.08 μmol L^{-1} and the analytical precision was better than ±2% (Han et al., 2012). The DO saturation degree (DO%) was the ratio of the observed DO to DO saturation, where the latter was calculated according to the empirical formula of Benson and Krause (1984).

2.3 Quantification of nutrient and carbonate dynamics with two or three end-member mixing models

A two or three end-member mixing model, as described in Dai et al. (2013), Cao et al. (2014) and Han et al. (2012), is used to predict their conservative concentrations and their comparisons with the measurements are used to quantify

https://engine.scichina.com/doi/10.1007/s11430-021-9963-8

nutrient and carbonate dynamics mediated by different processes. In a three end-member mixing model, the mixing scheme was established with salinity and potential temperature (θ) as conservative tracers:

$$S_1 \times F_1 + S_2 \times F_2 + S_3 \times F_3 = S_x, \quad (1)$$

$$\theta_1 \times F_1 + \theta_2 \times F_2 + \theta_3 \times F_3 = \theta_x, \quad (2)$$

$$F_1 + F_2 + F_3 = 1, \quad (3)$$

where S_x and θ_x are the salinity and potential temperature of the water samples; S_1, S_2, S_3 and θ_1, θ_2, θ_3 are the salinity and potential temperature of different end-members, respectively; F_1, F_2 and F_3 are the respective fractional contributions by different end-members. Note that TA is also frequently used as a conservative tracer in three end-member mixing models while salinity is typically used in two end-member mixing models given its conservative nature.

The concentration of a chemical (X, representing the DIC or PO_4^{3-} concentration) from the conservative mixing of these three different end-members ($X^{\text{conservative}}$) can be predicted as:

$$X^{\text{conservative}} = X_1 \times F_1 + X_2 \times F_2 + X_3 \times F_3. \quad (4)$$

Finally, in a three end-member mixing model, the difference between field measurements ($X^{\text{measurements}}$) and conservative values ($X^{\text{conservative}}$) obtained (defined as ΔX), as:

$$\Delta X = X^{\text{measurements}} - X^{\text{conservative}}, \quad (5)$$

where positive/negative values indicate non-conservative addition/removal of DIC and nutrients from other different sources/processes.

3. Results

3.1 Hydrographic setting

In the present study, the influence of coastal upwelling and plume water during both cruises was clearly reflected in the *T-S* diagrams and their spatial and cross-sectional distributions (Figures 2–7). In 2009, surface water with relatively low temperature (<28°C) and high salinity (>33) was observed at nearshore stations between the cities of Zhanjiang and Haikou (stations E500, QD02 and QD03) (Figure 2a, 2b), suggesting the influence of HNEU (Lin et al., 2016b). A similar *T-S* diagram for upwelled and offshore waters also confirmed the dominance of offshore subsurface water in the upwelling center (Figure 3a). In contrast, HNEU was not observed during the 2012 cruise, compounded by the fact that the area was covered by low salinity water (Lin et al., 2016a). However, upwelling evidenced by low sea surface temperature (SST, 25.4–27.0°C) and high sea surface salinity (SSS, >33) was observed at nearshore stations between the cities of Wenchang and Wanning (Figure 2d, 2e), indicating the appearance of HEU (Lin et al., 2016b).

In 2009, as reported by Yang et al. (2021), another water mass characterized by high SST (>29°C) and low SSS (<32) was detected at stations QD01, F45 and E600 along the coast between the cities Maoming and Zhanjiang (Figure 2a, 2b), and was very likely influenced by the plume water from local rivers (i.e., by coastal plume water, defined as salinity <33.0). The influence of this low salinity plume water is also evident in the *T-S* diagram in Figure 3a. In 2012, however, surface water characterized by exceptionally low salinity (<32.0) was also observed at nearshore station QD00 (Figure 2e), a result comparable to that obtained in 2009. In addition, plume water from the Pearl River characterized by low SSS (<32.0) and high SST (>29.3°C) was also observed at offshore stations along transect T0 (Figure 2d, 2e) (Dai et al., 2021), which was not observed in 2009.

3.2 Horizontal and vertical distributions of carbonate parameters

Horizontal and vertical distributions of temperature, salinity, DIC, TA and pH at 25°C ($pH_{@25}$), Ω_{arag} at 25°C ($\Omega_{arag@25}$), pCO_2 at 25°C ($pCO_{2@25}$) and pCO_2 at *in-situ* temperature ($pCO_{2@in\text{-}situ}$) in both cruises are shown in Figures 4–7. In 2009, SST ranged from 26.0 to 30.6°C, increasing with distance from shore (Figure 4a), and SSS varied 31.3 to 34.0 (Figure 4b). As mentioned earlier, high SST (>29.0°C) and low SSS (<33.0) at stations of QD01, F45 and E600 are indicative of coastal plume water; and low SST (<28°C) at stations E500, QD02 and QD03 is indicative of the influence of coastal upwelling. The range of DIC and TA was 1840–1940 and 2160–2230 μmol kg^{-1}, respectively, with high values in the upwelling area (1910–1940 μmol kg^{-1} for DIC and 2210–2230 μmol kg^{-1} for TA), associated with their high salinity (Figure 4b–4d). Low DIC and TA values were observed in coastal plume water (1840–1860 μmol kg^{-1} for DIC and 2160–2190 μmol kg^{-1} for TA) (Figure 4c, 4d). Low $pH_{@25}$ (8.03–8.08) and $\Omega_{arag@25}$ (3.05–3.35) were also observed in the upwelling area, but high $pH_{@25}$ (8.12–8.19) and $\Omega_{arag@25}$ (3.37–3.74) were observed in coastal plume water (Figure 4e, 4f). Similar $pCO_{2@25}$ and $pCO_{2@in\text{-}situ}$ distribution patterns were obtained with high values in the upwelling center (360–420 μatm) and low values in coastal plume water (300–360 μatm) (Figure 4g, 4h). Offshore, surface distributions of temperature, salinity, DIC, TA, $pH_{@25}$, $\Omega_{arag@25}$, $pCO_{2@25}$ and $pCO_{2@in\text{-}situ}$ exhibited a relatively uniform distribution pattern with a range of 29.0–30.3°C, 32.6–33.8, 1860–1890 μmol kg^{-1}, 2190–2220 μmol kg^{-1}, 8.10–8.15, 3.40–3.60, 280–340 μatm and 360–380 μatm, respectively (Figure 4a–4h).

Vertically, coastal plume water with low DIC and TA was observed in the upper mixed layer at stations E600 and QD01 along transects T1 and T2, associated with their low salinity (Figure 5). Additionally, high $pH_{@25}$ and $\Omega_{arag@25}$, and low $pCO_{2@25}$, and $pCO_{2@in\text{-}situ}$ were observed in coastal plume

https://engine.scichina.com/doi/10.1007/s11430-021-9963-8

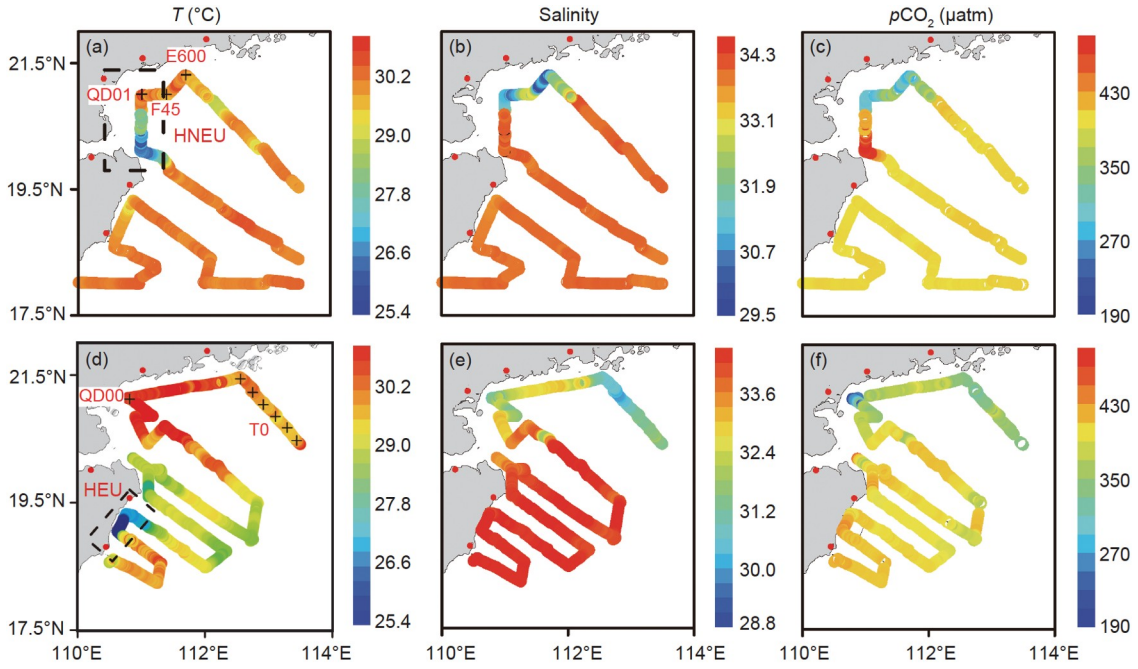

Figure 2 Surface distribution of temperature, salinity and carbon dioxide partial pressure (pCO_2) from measurements in 2009 ((a)–(c)) and 2012 ((d)–(f)). Red dots mark cities shown in Figure 1b. Crosses in (a) and (d) are sampling stations; HNEU and HEU are the same as in Figure 1.

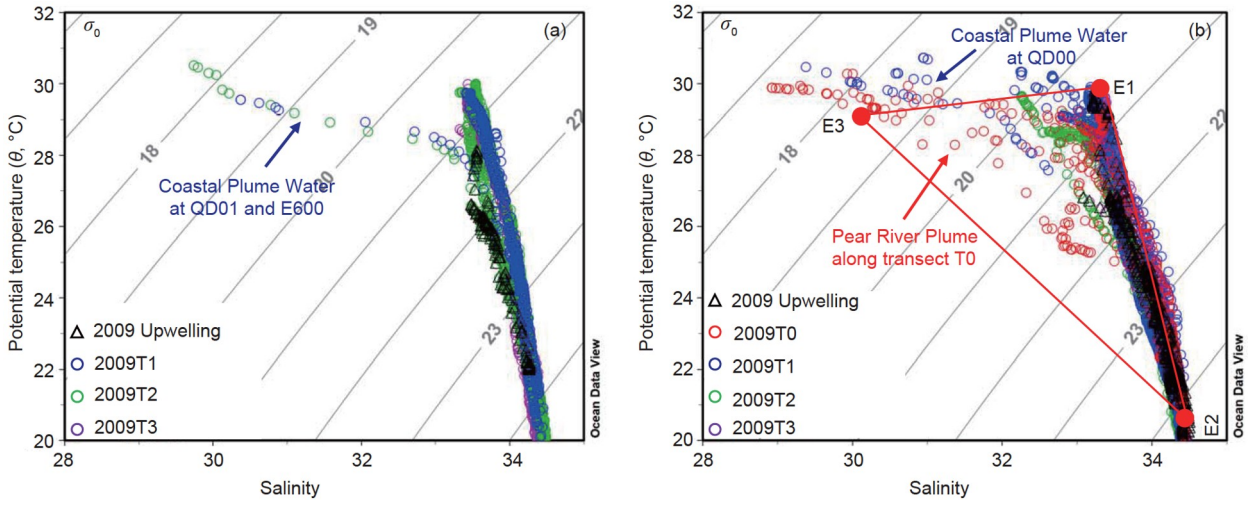

Figure 3 Relationship between potential temperature (θ, °C) and salinity (*T*-*S* diagram) in summers of 2009 (a) and 2012 (b). Open symbols are observed data in the indicated areas. Red solid circles in panel (b) are the end-members (i.e., E1 (Offshore Surface Water), E2 (Offshore Subsurface Water) and E3 (Plume Water)) used in the three end-member mixing model. Red solid lines represent the hypothetical conservative mixing lines between different end-members.

water as previously reported in the plume center in other river estuaries, such as the Changjiang Estuary and the Pearl River Estuary (Cao et al., 2011; Chou et al., 2013). It is important to note that the influence of coastal plume water was limited to the surface. Beneath the plume water, the influence of coastal upwelling was conspicuous, as evidenced by the shoreward transport of deep water with high salinity (>34) and low temperature (<21°C) that outcropped nearshore (Figure 5). In the upwelling system, high DIC, TA, $pCO_{2@25}$, and $pCO_{2@in\text{-}situ}$, and low $pH_{@25}$, and $\Omega_{arag@25}$ water parcels upwelled from the offshore subsurface, resulting in outcrops of CO_2-enriched subsurface water nearshore, as previously reported (Dong et al., 2017).

In 2012, SST and SSS exhibited a range of 25.4–30.6°C and 29.0–34.0, respectively (Figure 6a, 6b). At HEU, surface water in the upwelling system was characterized by low SST (<27.0°C) and high SSS (>33.5). In contrast, surface water at QD00 was influenced by the coastal plume water, and at offshore stations along transect T0 was influenced by the Pearl River Plume characterized by high temperature (>29.0°C) and low salinity (<31.0), as noted in previous studies (Cao et al., 2011; Lin et al., 2016b; Dai et al., 2021;

https://engine.scichina.com/doi/10.1007/s11430-021-9963-8

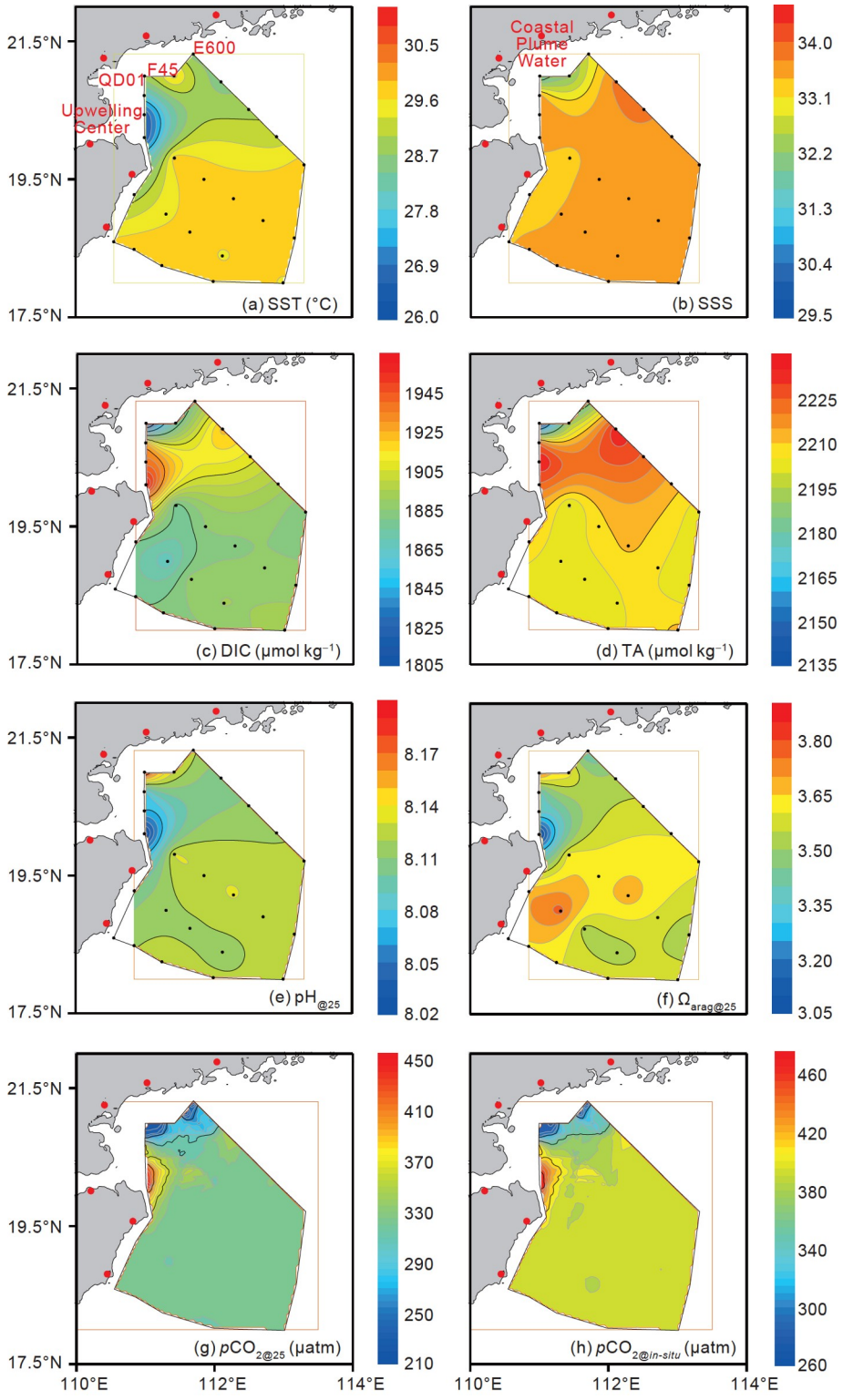

Figure 4 Sea surface distribution of (a) temperature, SST, (b) salinity, SSS, (c) dissolved inorganic carbon, DIC, (d) total alkalinity, TA, (e) $pH_{@25}$, (f) $\Omega_{arag@25}$, (g) $pCO_{2@25}$ and (h) $pCO_{2@in\text{-}situ}$ in 2009. Salinity and temperature are surface data obtained at 1 m using CTD; $pCO_{2@in\text{-}situ}$ is obtained with a continuous-flow underway system; $pCO_{2@25}$ represents pCO_2 values normalized to 25°C, following method of Takahashi et al. (1993). Red dots mark cities shown in Figure 1b.

Yang et al., 2021). In coastal plume water, surface water was characterized by low DIC (<1780 μmol kg^{-1}), TA (<2100 μmol kg^{-1}), $pCO_{2@25}$ (<280 μatm) and $pCO_{2@in\text{-}situ}$ (<280 μatm), and high $pH_{@25}$ (>8.10) and $\Omega_{arag@25}$ (>3.60) (Figure 6c–6h). Additionally, low DIC (1780–1840 μmol kg^{-1}) and TA (2090–2150 μmol kg^{-1})

https://engine.scichina.com/doi/10.1007/s11430-021-9963-8

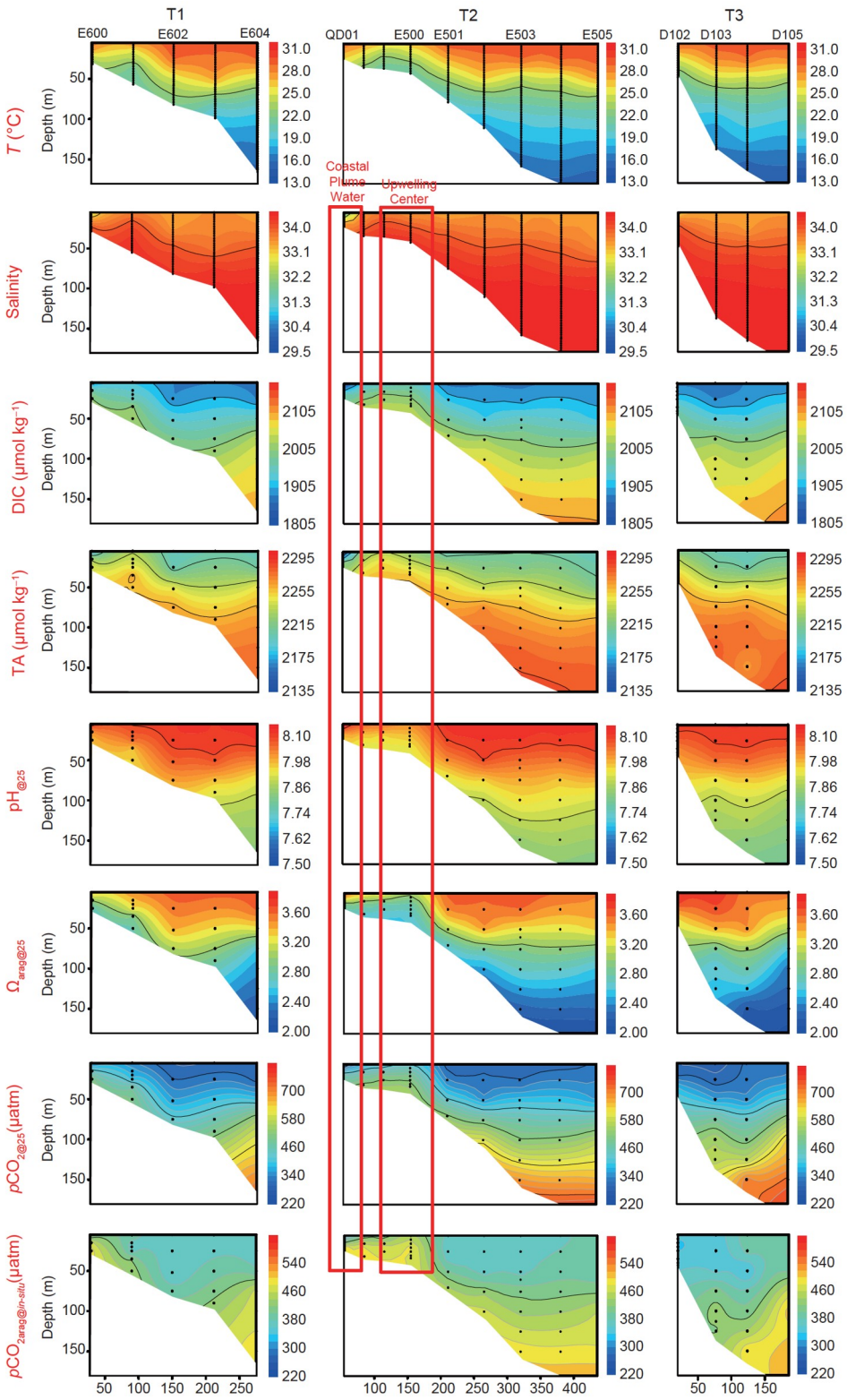

Figure 5 Vertical distributions of temperature, salinity, dissolved inorganic carbon (DIC), total alkalinity (TA), $pH_{@25}$, $\Omega_{arag@25}$, $pCO_{2@25}$ and $pCO_{2@in\text{-}situ}$ (definition of parameters as in Figure 4) along different transects (T1 to T3) in 2009. Salinity and temperature are obtained from 1 m using CTD. Upwelling Center and Coastal Plume Water are marked with red rectangles.

(Figure 6c, 6d) were also observed in the Pearl River Plume, while $pH_{@25}$, $\Omega_{arag@25}$, $pCO_{2@25}$ and $pCO_{2@in\text{-}situ}$ values were comparable to those of offshore surface water (Figure 6e–6h). Surface water characterized by high DIC (1870–1930 μmol kg^{-1}), TA (2180–2220 μmol kg^{-1}), $pCO_{2@25}$ (360–380 μatm) and $pCO_{2@in\text{-}situ}$ (380–420 μatm),

https://engine.scichina.com/doi/10.1007/s11430-021-9963-8

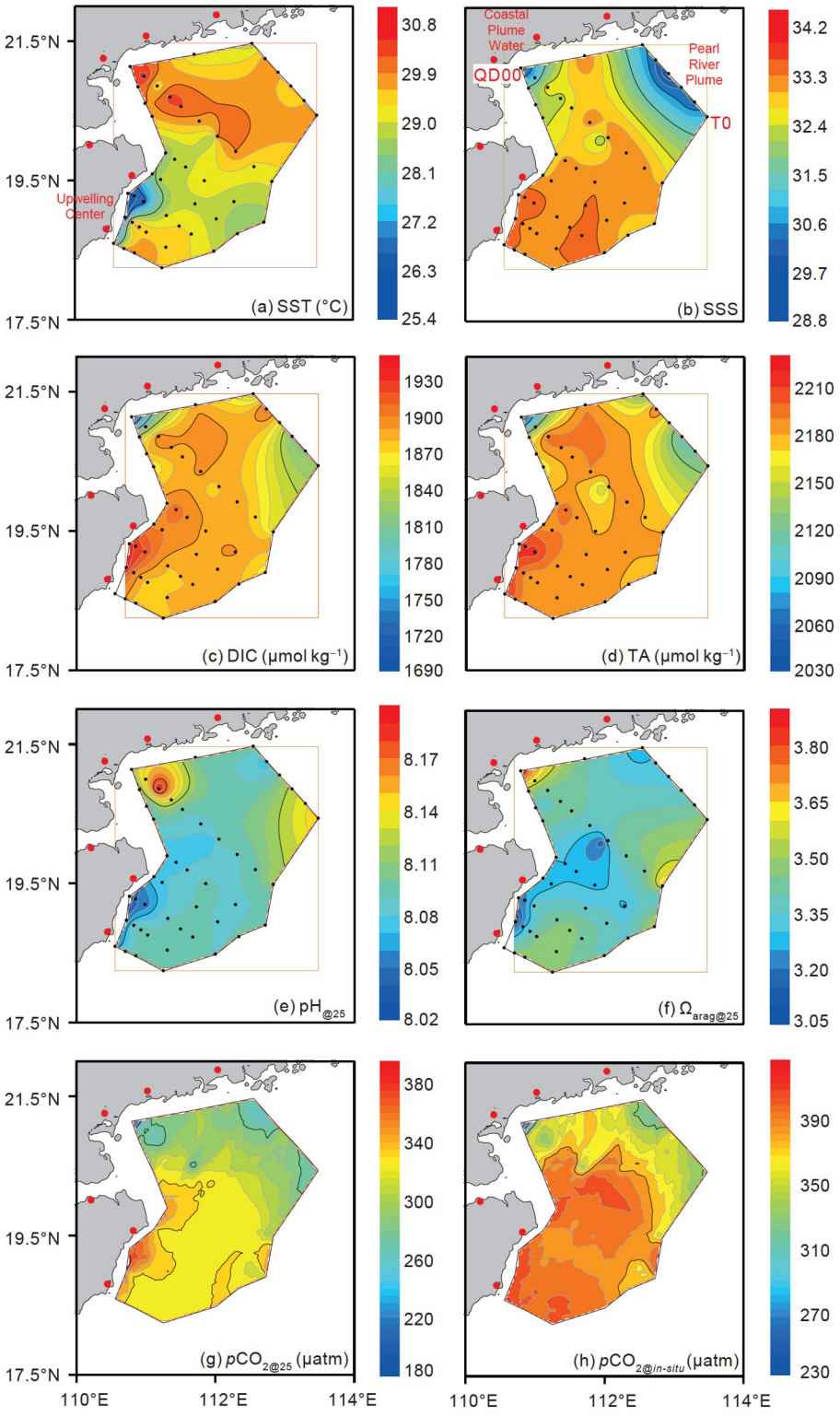

Figure 6 Sea surface distributions of (a) temperature, SST, (b) salinity, SSS, (c) dissolved inorganic carbon, DIC, (d) total alkalinity, TA, (e) $pH_{@25}$, (f) $\Omega_{arag@25}$, (g) $pCO_{2@25}$ and (h) $pCO_{2@in\text{-}situ}$ (see text for definition of parameters) in 2012. Salinity and temperature are surface data obtained at 1 m using CTD. $pCO_{2@in\text{-}situ}$ is obtained with a continuous-flow underway system. $pCO_{2@25}$ are the pCO_2 measurements normalized to 25°C following method of Takahashi et al. (1993). Red dots mark cities shown in Figure 1b.

and low $pH_{@25}$ (8.03–8.06) and $\Omega_{arag@25}$ (3.10–3.30) values, was observed at HEU (Figure 6c–6h), suggesting the influence of CO_2-enriched subsurface water. Offshore, temperature, salinity, DIC, TA, $pH_{@25}$, $\Omega_{arag@25}$, $pCO_{2@25}$ and $pCO_{2@in\text{-}situ}$ in surface water varied in the range 27.8–30.2°C, 32.8–33.8, 1850–1880 μmol kg^{-1}, 2180–2215 μmol kg^{-1},

https://engine.scichina.com/doi/10.1007/s11430-021-9963-8

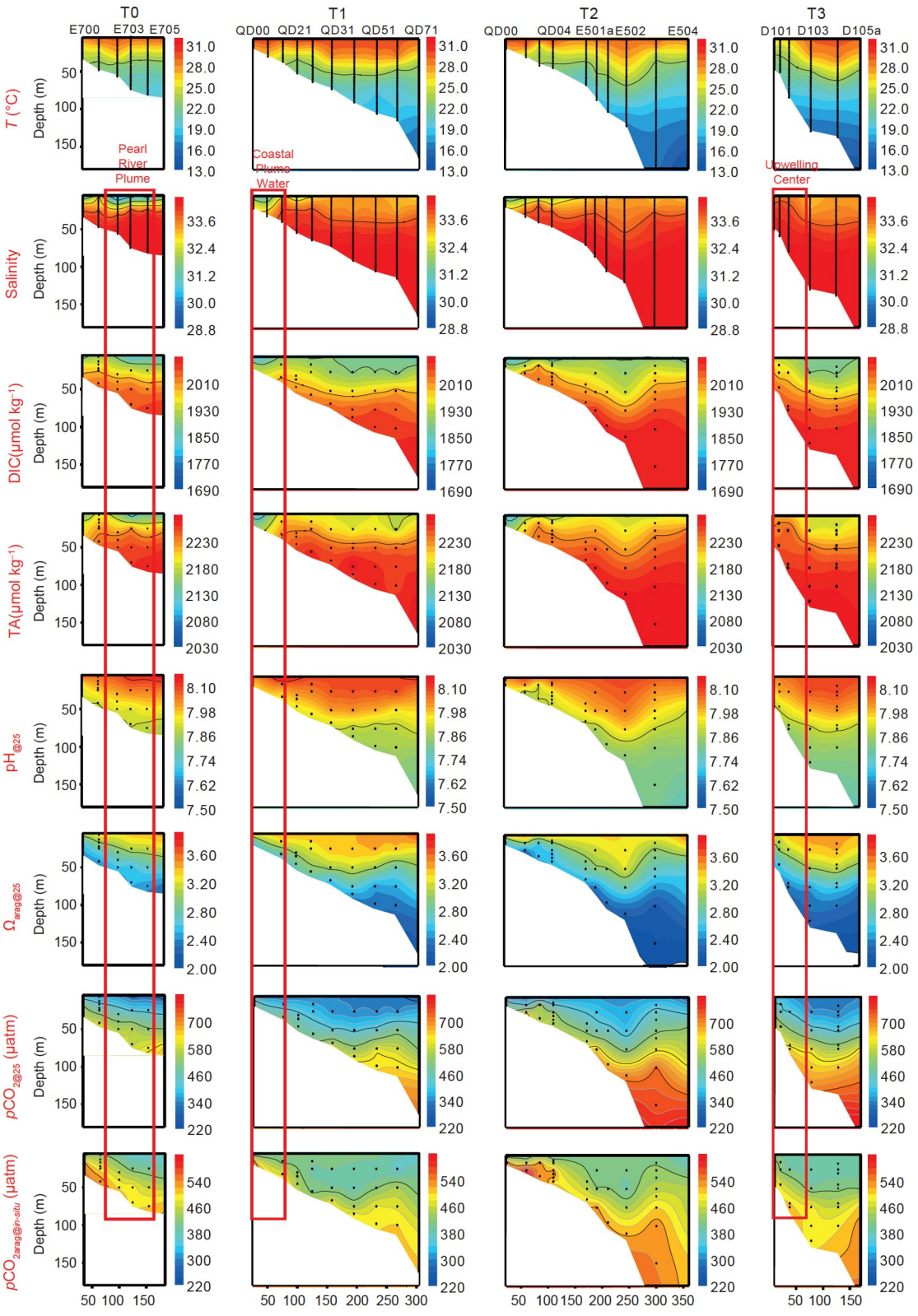

Figure 7 Vertical distributions of temperature, salinity, dissolved inorganic carbon (DIC), total alkalinity (TA), $pH_{@25}$, $\Omega_{arag@25}$, $pCO_{2@25}$ and $pCO_{2@in\text{-}situ}$ (parameters defined as in Figure 4) along different transects (T0 to T3) in 2012. Salinity and temperature were obtained at 1 m using CTD. Upwelling Center, Coastal Plume Water and Pearl River Plume are marked with red rectangles.

8.08–8.12, 3.40–3.55, 300–350 μatm and 380–410 μatm, respectively, with a rather uniform distribution pattern (Figure 6a–6h). Vertically, the influence of plume water resulted in low DIC, TA, $pCO_{2@25}$ and $pCO_{2@in\text{-}situ}$, and high

https://engine.scichina.com/doi/10.1007/s11430-021-9963-8

$pH_{@25}$ and $\Omega_{arag@25}$ values in the upper mixed layer at offshore stations along transect T0 and at station QD00 (Figure 7). At nearshore stations along transect T3, the uplifted isopleths of DIC, TA, $pH_{@25}$, $\Omega_{arag@25}$, $pCO_{2@25}$ and $pCO_{2@in\text{-}situ}$ suggested upwelling of CO_2-enriched subsurface water from offshore (Figure 7).

4. Discussion

4.1 Variability of river plumes in the NWSCS

The occurrence of river plumes is frequently reported in coastal areas in the NWSCS (Lin et al., 2016b; Dong et al., 2017; Yang et al., 2021). In 2009, the coastal plume water TA-S relationship was described by the linear equation y=36.7x+1088 (coefficient of determination, R^2=0.81). Prior studies suggested that TA concentrations from the freshwater end-member in the mainland (such as the Jianjiang River) and from Hainan Island (e.g., the Wanquan and Wenchang Rivers) varied over a narrow range of 460–737 μmol kg^{-1} (Dai et al., unpublished data; Dong et al., 2017). The observed TA intercept was much higher than that of the freshwater end-member of coastal local rivers, indicating contributions of other TA sources. In coastal plume water at surface, the activities of ^{226}Ra and ^{228}Ra (in dpm 100 L^{-1}) ranged from 8.5 to 12.5 and from 20.0 to 30.0, respectively, which was much higher than those in offshore surface water (Wang et al., unpublished data). Relatively high $^{228}Ra/^{226}Ra$ ratios, 2.93 to 3.59, were also observed in coastal plume water. Among the potential sources of radium to this region, the average $^{228}Ra/^{226}Ra$ ratio of coastal local rivers was 2.52 ±0.02, and that of coastal groundwater was 7.68±2.24 (Dai et al., 2021). Thus, such high $^{228}Ra/^{226}Ra$ ratios in coastal plume water must have resulted from submarine groundwater discharge. In this region (e.g., station QD01), the influence of submarine groundwater discharge can be discerned in the whole water column from the relatively high $^{228}Ra/^{226}Ra$ ratios (Wang et al., unpublished data).

In 2012, two low salinity water parcels were observed at station QD00 and at offshore stations along transect T0. At station QD00, a linear regression provided a good fit to the water column relationship between TA and salinity (y=44.4x +700, R^2=0.94). The intercept was consistent with the freshwater end-member of coastal local rivers (Dai et al., unpublished data; Dong et al., 2017), thus confirming the influence of coastal plume water in 2012 as suggested by Lin et al. (2016b). For the upper water column along transect T0, a very good linear relationship was found between TA and S (y=33.5x+1232, R^2=0.90), the intercept of which is consistent with the Pearl River freshwater end-member that ranged seasonally from 1190 to 2114 μmol kg^{-1} (Guo et al., 2008). This confirms the influence of the Pearl River Plume as suggested by Dai et al. (2021).

To clarify the general effect of freshwater from coastal rivers, Lin et al. (2016b) computed the precipitation rate during these two summer cruises. Their results suggested that, in 2009, high precipitation rate in the Leizhou Peninsula brings considerable freshwater to nearshore areas off the northeastern coast of Hainan Island, resulting in a low-salinity, nearshore surface water mass, whereas the discharge from coastal rivers was much lower in 2012. Thus, the plume area influenced by coastal plume water was larger in 2009 than in 2012.

To examine the influence of the Pearl River Plume during both cruises, surface distributions of temperature and salinity during the summers of 2009 and 2012 are shown for the entire northern shelf in Appendix Figure S1 (https://link.springer.com). Results showed that the Pearl River Plume was observed on the northeastern shelf in 2009, and on the northwestern shelf in 2012. On the northern shelf, the orientation of the Pearl River Plume is suggested to be modulated mainly by the wind field (Dong et al., 2004; Ou et al., 2009; Xu et al., 2019). When southeasterly and easterly winds prevail, the Pearl River Plume generally extends along the western coast under the influence of the wind-driven westward coastal current and shoreward Ekman transport, and thus plume water is observed on the northwestern part of the shelf. In contrast, when southerly and southwesterly winds prevail, the Pearl River Plume typically expands in an eastward direction, which is often observed on the northeastern part of the shelf (Dong et al., 2004; Gan et al., 2009; Ou et al., 2009; Xu et al., 2019). In 2009, the Pearl River Plume was observed on the shelf on July 20. Subsequently, forced by southerly winds during July 20–25, surface plume water was transported eastwardly, and the plume center was observed on the northeastern shelf on July 25 (Appendix Figure S2b, S2c). The movement of plume water was also tracked by the currents (Appendix Figure S2b, S2c). In 2012, the Pearl River Plume characterized by high SST was observed in the Pearl River Estuary on August 3 (Appendix Figure S2f), and subsequently it was transported southward under the prevailing northwesterly wind stress, and plume water was finally observed on the northwestern offshore shelf on August 8 (Appendix Figure S2g).

It is interesting to note that the plume area influenced by the Pearl River was larger in 2012 than in 2009 during the cruises (Appendix Figure S1), whilst the freshwater discharge rate in Xijiang River (the largest river of the Pearl River system) for the period from July 10 to August 10 before and during sampling in 2012 was lower, ~69% of the 2009 average discharge (for the period from June 28 to July 28 before and during sampling). This suggests that the plume area is not only determined by the river discharge rate but also influenced by the wind filed (e.g., Chen et al., 2017; Fong and Geyer, 2001). Zu et al. (2014) also reported a larger plume area with a smaller river discharge rate on the

https://engine.scichina.com/doi/10.1007/s11430-021-9963-8

northeastern shelf, which was mediated by both wind stress and river discharge. We contend that the tendency of the surface plume range to increase due to wind mixing far exceeded the tendency for it to shrink caused by reduced river discharge (Zu et al., 2014).

4.2 Processes controlling sea surface pCO_2 dynamics in the NWSCS

As shown in Figure 2, the distributions of sea surface pCO_2 ($pCO_{2@in\text{-}situ}$) showed high spatial variability. During both cruises, the highest pCO_2 values (>400 μatm) were observed in the upwelling center, whereas the lowest values (<350 μatm) were observed in the plume water. Offshore, the sea surface pCO_2 range was 360–410 μatm with a fairly uniform distribution pattern (Figure 2c, 2f). To identify the effects of temperature and water mass mixing on the dynamics of sea surface pCO_2, the logarithm relationship between sea surface pCO_2 and SST ($\ln pCO_2$-SST) and between temperature-normalized sea surface pCO_2 ($npCO_2$) and SSS ($npCO_2$-SSS) were plotted in Figure 8. An annual average SST of 26°C was used for temperature normalization (Zhai et al., 2005a, 2013), following method of Takahashi et al. (1993).

The lower and upper limit of the annual average sea surface pCO_2 on the northern South China Sea shelf, 350 and 390 μatm (Zhai et al., 2005a, 2013), respectively, are the intercepts of the linear regression equations indicated by the black dashed lines in Figure 8a, 8c. If the observed pCO_2 varies between these two dashed lines, sea surface pCO_2 is thus mainly controlled by temperature. In turn, for pCO_2 values higher/lower than the upper/lower dashed line, other effects, may override temperature effects in regulating sea surface pCO_2. During both cruises, most pCO_2 measurements from the upwelling and offshore areas occurred above or below these two dashed lines, leading to the conclusion that non-temperature effects were the main contributors to the spatial dynamics of sea surface pCO_2.

In Figure 8b, 8d, $npCO_2$ in the upwelling area during both cruises is much higher than in the other sub-regions, supporting the dominance of upward transport of CO_2-enriched subsurface water in upwelling systems (Cao et al., 2011; Xue et al., 2016). In the Pearl River Plume (Figure 10d) and coastal plume water during both cruises (Figure 8b, 8d), the constrained $npCO_2$-SSS relationships suggest that the mixing of plume water was characterized by low SSS and $npCO_2$, while offshore surface water exhibited high SSS and $npCO_2$. Thus, water mass mixing may dominate the spatial dynamics of sea surface pCO_2 in these sub-regions. In contrast, offshore $npCO_2$ is nearly constant during both cruises, showing that water mass mixing plays a minor role in regulating sea surface pCO_2.

Finally, phytoplankton production may also contribute to the spatial dynamics of sea surface pCO_2. In coastal plume water and the Pearl River Plume, supersaturated DO (DO% >110%) was determined in surface water (Figure 9e, 9f), indicating relatively high phytoplankton production in these sub-regions, which may also contribute to the low pCO_2. To evaluate the dynamics of sea surface pCO_2 attributed to

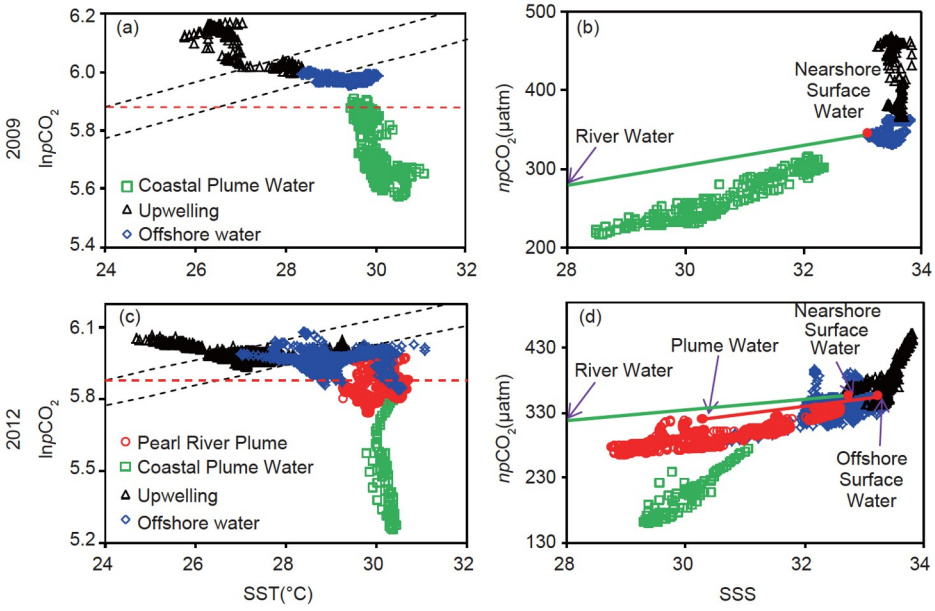

Figure 8 Relationships of $\ln pCO_2$ vs. sea surface temperature, SST ($\ln pCO_2$-SST, left panels) and $npCO_2$ vs. sea surface salinity, SSS ($npCO_2$-SSS, right panels) for surface waters in 2009 ((a), (b)) and 2012 ((c), (d)). In panels (a) and (c), red dashed lines indicate the logarithm of air pCO_2, and the two black dashed lines encompass an area where temperature dominates sea surface pCO_2 variability (see text for details). In panels (b) and (d), red dots represent the end-members of Offshore Surface Water, Plume Water, River Water and Nearshore Surface Water as shown in Table 1; green and red solid lines represent the hypothetical conservative mixing lines between different end-members. In panels (c) and (d), red circles are the measurements in the Pearl River Plume.

https://engine.scichina.com/doi/10.1007/s11430-021-9963-8

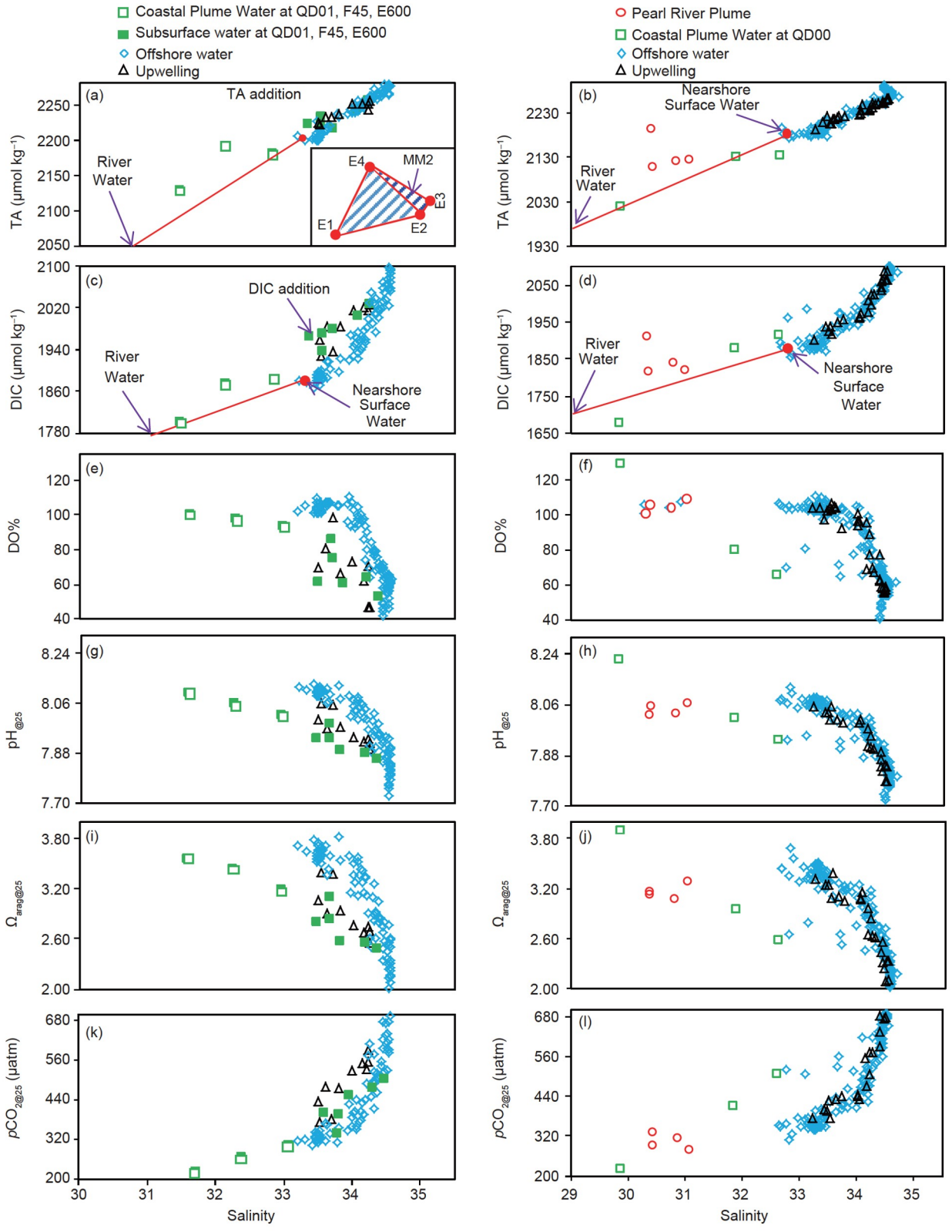

Figure 9 TA-Salinity, S ((a), (b)), DIC-S ((c), (d)), DO%-S ((e), (f)), $pH_{@25}$-S ((g), (h)), $\Omega_{arag@25}$-S ((i), (j)) and $pCO_{2@25}$-S ((k), (l)) relationships in summer 2009 (left panels) and 2012 (right panels) in various indicated locations. In panels (a)–(d), red dots represent the end-members of River Water (E1), Nearshore Surface Water (E2), Nearshore Subsurface Water (E3), and Submarine Groundwater Discharge (E4) as shown in Table 1; red solid lines represent the hypothetical conservative mixing lines between different end-members. Also shown in panel (a) are the three end-member mixing model of River Water, Nearshore Surface Water and Submarine Groundwater Discharge in Coastal Plume Water (mixing model 1, MM1) and the mixing of Nearshore Surface Water, Nearshore Subsurface Water and Submarine Groundwater Discharge in upwelling waters (mixing model 2, MM2).

https://engine.scichina.com/doi/10.1007/s11430-021-9963-8

phytoplankton production, hypothetical relationships of $npCO_2$ vs. SSS in Offshore Surface Water, Plume Water, River Water and Nearshore Surface Water were also plotted (Figure 8b, 8d); their end-member values are summarized in Table 1. Results of this analysis indicated that in coastal plume water during both cruises, the $npCO_2$ values from field measurements were much lower than along the conservative mixing line, suggesting pCO_2 drawdown attributed to high phytoplankton production. In the Pearl River Plume, lower $npCO_2$ values than along the conservative mixing line were also observed, but the pCO_2 drawdown was much weaker than in coastal plume water.

In Figure 8a, 8c, if pCO_2 measurements are higher (lower) than the air pCO_2, the area acts as a CO_2 source (sink), resulting in a decrease (increase) of DIC and sea surface pCO_2. Thus, CO_2 outgassing will result in drawdown of sea surface pCO_2 in both upwelling and offshore areas, while CO_2 intrusion will raise sea surface pCO_2 in the Pearl River Plume and coastal plume water.

4.3 Dynamics of the carbonate system mediated by river plumes, biological processes and submarine groundwater discharge in the NWSCS

4.3.1 Dynamics of the carbonate system in River plumes

As shown in section 4.1, the coastal plume water in 2009 was influenced by the submarine groundwater discharge. High DO%, $pH_{@25}$ and $\Omega_{arag@25}$, and low $pCO_{2@25}$ were also determined in this low salinity plume water (Figure 9e, 9g, 9i, 9k), indicative of high phytoplankton production. At the surface, coastal plume water seemed to be controlled by River Water, Nearshore Surface Water and Submarine Groundwater Discharge water masses, and the dynamics of carbonate parameters were thus quantified using a three end-member mixing model using salinity and TA as tracers (see MM1 in Figure 9a). Using end-members summarized in Table 1, the contribution of submarine groundwater discharge ranged from 0.5% to 1.5% in surface water, with an average of 0.9±0.5%. Wang et al. (unpublished data) also quantified the fractions of submarine groundwater discharge during the same cruise using a three end-member mixing model with tracers of long-lived radium isotopes (^{226}Ra and ^{228}Ra). Their result shows that the proportion of groundwater ranged from 0.1% to 1.4% in the coastal plume water with an average of 0.8±0.4%, agreed rather well with our calculations. Based on the high DIC and TA concentrations in the submarine groundwater discharge end-member, the DIC and TA additions from submarine groundwater discharge were estimated at 38.9±20.5 μmol kg^{-1} (range=18.5–59.4 μmol kg^{-1}) and 42.5±22.3 μmol kg^{-1} (range=20.1–64.8 μmol kg^{-1}), respectively. Finally, DIC removal of 10.0±10.4 μmol kg^{-1} is estimated to balance the DIC budget, which was probably attributable to the high phytoplankton DIC uptake in plume water.

To further quantify the dynamics of pH, Ω_{arag} and pCO_2 mediated by submarine groundwater discharge and the phytoplankton production, the following predictions based on a three end-member mixing model were made below. Firstly, we calculated the conservative DIC following method described in Section 2.3 (defined as $DIC^{conservative}$), and pH, Ω_{arag} and pCO_2 calculated from $DIC^{conservative}$ and $TA^{measurements}$ at 25°C were obtained with the CO2SYS program (defined as $pH^{conservative}$, $\Omega_{arag}{}^{conservative}$ and $pCO_2{}^{conservative}$, respectively). Secondly, DIC and TA additions from submarine groundwater discharge (SGD) were subtracted from $DIC^{conservative}$ and $TA^{measurements}$ (defined as $DIC^{conservative-SGD}$ and

Table 1 Summary of end-member values of the properties of water masses in sub-regions influenced by Coastal Plume Water and coastal upwelling in 2009, and by Coastal Plume Water and the Pearl River Plume in 2012[a)]

Cruise	End-members	Potential temperature (°C)	Salinity	DIC (μmol kg^{-1})	TA (μmol kg^{-1})
2009	River water		0	522.5	500.7
	Nearshore subsurface water	21.8	34.3	2008.9	2262.7
	Nearshore surface water	28.8	33.2	1879.7	2207.0
	Submarine groundwater discharge	22.5	24.3	4054.9	4420.4
2012	River water		0	522.5	500.7
	Plume water	29.3	30.3	1815.0	2105.5
	Offshore surface water	29.9	33.3	1888.1	2191.4
	Offshore subsurface water	20.6	34.4	2031.0	2252.0
	Nearshore surface water	29.3	32.6	1896.0	2196.0

a) The River Water end-member was obtained from Dai et al. (unpublished data) and Dong et al. (2017), while Plume Water is the average of low salinity surface water (~5 m) in the plume center. Value of the Offshore Surface Water end-member is the average of offshore data at 5 m depth, and the Offshore Subsurface Water end-member is the average of data at ~50–70 m depth (see text). Nearshore Surface Water value correspond to those of surface water (~5 m) at stations D102 in 2009 and QD21a in 2012; Nearshore Subsurface Water value correspond to those of subsurface water (~35 m) at station E601. The Submarine Groundwater Discharge end-member was obtained from Wang et al. (unpublished data). DIC=dissolved inorganic carbon, TA=total alkalinity.

https://engine.scichina.com/doi/10.1007/s11430-021-9963-8

$TA^{measurements-SGD}$), and pH, Ω_{arag} and pCO_2 were subsequently calculated from $DIC^{conservative-SGD}$ and $TA^{measurements-SGD}$ at 25°C (defined as $pH^{conservative-SGD}$, $\Omega_{arag}{}^{conservative-SGD}$ and $pCO_2{}^{conservative-SGD}$, respectively). Their differences are the deviations attributed to submarine groundwater discharge. Thirdly, the difference in pH, Ω_{arag} and pCO_2 between the field measurements at 25°C (defined as $pH^{measurements}$, $\Omega_{arag}{}^{measurements}$ and $pCO_2{}^{measurements}$, respectively) and the conservative values ($pH^{conservative}$, $\Omega_{arag}{}^{conservative}$ and $pCO_2{}^{conservative}$) were obtained, which are attributed to phytoplankton production. As a result, predicted changes in pH, Ω_{arag} and pCO_2 attributed to submarine groundwater discharge were relatively minor (<0.01 for pH, <0.10 for Ω_{arag} and <10 μatm for pCO_2), and DIC and TA additions followed a ratio of ~0.92, while the high phytoplankton production in coastal plume water would reduce the pCO_2 by 14.3±14.2 μatm (range=1.3–29.0 μatm) and increase the pH and Ω_{arag} by 0.02±0.02 (range=0–0.04) and 0.11±0.11 (range=0.01–0.22), respectively.

In 2012, the influence of coastal plume water was also observed at station QD00. A two end-member mixing model between River Water and Nearshore Surface Water was established (Figure 9b, 9d). In surface water, the observed TA was almost exclusively on the mixing line, while observed DIC was much lower than the mixing line, suggesting DIC consumption via phytoplankton production. Associated with this DIC consumption, high DO%, $pH_{@25}$ and $\Omega_{arag@25}$, and low $pCO_{2@25}$ were indeed consistently observed (Figure 9f, 9h, 9j, 9l). In the coastal plume water, DIC removal via strong phytoplankton production was estimated at 104.2 μmol kg^{-1} at the surface, which drew down the sea surface pCO_2 by 111.1 μatm but augmented pH and Ω_{arag} by 0.13 and 0.73, respectively. It is noteworthy that in coastal plume water the influence of submarine groundwater discharge was only observed in 2009, suggesting temporal variability of the submarine groundwater discharge with varying precipitation rates that is in agreement with previous reports (Liu et al., 2012; Wang et al., 2014; Tan et al., 2018).

In the Pearl River Plume during 2012, the dynamics of TA, DIC and other carbonate parameters was likely controlled by mixing of different water masses and subsequently by the high phytoplankton production supported by nutrients from different end-members that showed high DO%, $pH_{@25}$ and $\Omega_{arag@25}$, and low $pCO_{2@25}$ (Figure 9f, 9h, 9j, 9l). Three end-members were identified from the *T-S* relationship: Plume Water, Offshore Surface Water and Offshore Subsurface Water (Figure 3b). Below we quantify DIC dynamics using a three end-member mixing model with potential temperature and salinity as tracers as described in section 2.3. Since air-water CO_2 exchange has no effect on TA, we validated the model with TA. The resulting model-derived values are in good agreement with field observations with uncertainties averaging 3.2±5.3 μmol kg^{-1}, thus strongly supporting our model predictions. In surface water, the non-conservative portion of DIC (ΔDIC) and nutrients (ΔPO_4) during mixing of different water masses were obtained. Total ΔDIC is 18.7±20.2 μmol kg^{-1}, a net result of biological activity and air-sea CO_2 exchange. Biological uptake of PO_4^{3-} is 0.1±0.1 μmol kg^{-1}, and thus DIC photosynthetic consumption (calculated as $106\Delta PO_4$ based on the classic Redfield ratio (Redfield et al., 1963) is 7.9±6.0 μmol kg^{-1}. To balance the DIC budget, DIC addition induced by air-sea CO_2 exchange is estimated as 26.5±19.5 μmol kg^{-1}.

In the Pearl River Plume, average (±SD) sea surface pCO_2, pH and Ω_{arag} due to conservative mixing, calculated from $DIC^{conservative}$ and $TA^{conservative}$ at the *in-situ* temperature using CO2SYS software, were 379.5±14.2 μatm, 8.05±0.01 and 3.43±0.05, respectively. Then, biological uptake supported by the nutrients in different end-members would draw down the pCO_2 by 4.3±4.2 μatm and increase the pH and Ω_{arag} by 0.01±0.01 and 0.02±0.02, respectively. Finally, CO_2 uptake in plume water would level up sea surface pCO_2 by 10.4 ±15.3 μatm and draw down pH and Ω_{arag} by 0.01±0.01 and 0.06±0.09, respectively, based on DIC mass balance.

4.3.2 Dynamics of the carbonate system in upwelling

Rather different from the upwelled waters in 2012 where carbonate dynamics was dominated by the shoreward transport of offshore water without the influence of other water masses, the upwelled waters in 2009 was characterized by the influence of a water mass of high DIC, TA and $pCO_{2@25}$, and low DO%, $pH_{@25}$ and $\Omega_{arag@25}$ (Figure 9a, 9c, 9e, 9g, 9i, 9k). In 2009, similar to observations in coastal plume water at stations QD01, F45 and E600, surface water in the upwelling center (stations E500, QD02 and QD03) was characterized by higher ^{226}Ra and ^{228}Ra activities than offshore surface water (Wang et al., unpublished data). The observed higher $^{228}Ra/^{226}Ra$ ratios (~2.85) than the end-member of coastal local rivers (2.52±0.02) suggested the influence of submarine groundwater discharge at the surface (Dai et al., 2021). Vertically, in the upwelling center, surface and subsurface ^{228}Ra activities and $^{228}Ra/^{226}Ra$ ratios were higher than in bottom water (e.g., station E500, Wang et al., unpublished data), suggesting that submarine groundwater discharge additions occurred at the surface and subsurface transported from inshore waters. Thus, the influence of submarine groundwater discharge on DIC and TA dynamics could be estimated using a three end-member mixing model with salinity and TA as tracers, and a mixing scheme between Nearshore Surface Water, Nearshore Subsurface Water and submarine groundwater discharge (as shown in Figure 9a, see MM2). Using the end-members summarized in Table 1, the contribution of submarine groundwater discharge ranged from 0.1% to 0.9%, and averaged 0.5±0.3%, agreed rather well with results from a three end-member mixing model with tracers of ^{226}Ra and ^{228}Ra (ranged from

https://engine.scichina.com/doi/10.1007/s11430-021-9963-8

0.3% to 1.1% with an average of 0.6±0.3%) (Wang et al., unpublished data). Mean DIC and TA additions from submarine groundwater discharge were estimated at 22.3±12.6 μmol kg^{-1} (range=4.7–37.9 μmol kg^{-1}) and 24.3±13.8 μmol kg^{-1} (range=5.1–41.3 μmol kg^{-1}), respectively. Finally, a DIC addition of 23.8±8.4 μmol kg^{-1} (range =11.8–33.6 μmol kg^{-1}) was required to balance the DIC budget, was an addition probably attributable to DIC regeneration resulting from organic matter remineralization (Sunda and Cai, 2012; Su et al., 2017).

Additionally, the dynamics of pH, Ω_{arag} and pCO_2 mediated by submarine groundwater discharge and organic matter remineralization were quantified. The additions of submarine groundwater discharge made a minor contribution to the variability of pH, Ω_{arag} and pCO_2 (<0.01 for pH, <0.10 for Ω_{arag} and <10 μatm for pCO_2), a result consistent with that in coastal plume water in 2009. Thus, the dynamics of pH, Ω_{arag} and pCO_2 in upwelling waters were mostly attributed to organic matter remineralization, which would draw down the pH and Ω_{arag} by 0.04±0.04 (range=0.02–0.06) and 0.24±0.09 (range=0.12–0.35), respectively, but increase the seawater pCO_2 by 63.4±32.2 μatm (range=22.5–103.3 μatm).

4.4 Future scenarios of seawater acidification resulting from multiple drivers

As shown in section 4.3, the dynamics of the carbonate system in the NWSCS was mainly controlled by plume water from coastal local rivers, submarine groundwater discharge and organic matter remineralization. Additionally, increasing atmospheric CO_2 may facilitate its dissolution in seawater (Chou et al., 2013; Wang et al., 2014). However, the increasing seawater temperature may level up the seawater pCO_2, and partially cancel off the CO_2 sink (Chou et al., 2013; McNeil and Matear, 2007). In the present study, we predict pH and Ω_{arag} in the NWSCS under the interaction of increasing atmospheric CO_2 and seawater temperature, river plume effects, submarine groundwater discharge influence and organic matter remineralization in 2100 with the following assumptions.

Firstly, due to the fact that the carbonate system for the entire water column at nearshore stations (<100 m depth) without the influence of coastal plume water and submarine groundwater discharge in 2009 is consistent with 2012, the nearshore carbonate system in 2009 is taken as the reference condition. Secondly, we assume that seawater pCO_2 is in equilibrium with atmospheric CO_2, and air CO_2 concentration would be 800 ppm (1 ppm=1×10^{-6}) in 2100 (Chou et al., 2013; Wang et al., 2014). In addition, the sea surface temperature increases is assumed to be 2°C (Chou et al., 2013; McNeil and Matear, 2007). Thirdly, we assume that DIC and TA additions from submarine groundwater discharge remain unchanged, which equals ~40 μmol kg^{-1}. Next, we assume strong biological respiration in submarine groundwater discharge, which would raise the DIC concentration by ~24 μmol kg^{-1}. Finally, we assume strong phytoplankton production in surface plume water, which will likely generate more organic matter and its sinking to bottom water for further decomposition (Sunda and Cai, 2012; Chou et al., 2013; Su et al., 2017). Given the DIC consumption of ~104.2 μmol kg^{-1} in the surface water of the coastal plume water and 60% of the marine sources organic carbon settled to the subsurface and bottom water (Wu et al., 2017), remineralization of this organic carbon would increase DIC concentrations by ~60 μmol kg^{-1} in bottom waters.

Our prediction showed that in 2100, the CO_2 sequestration regulated by both the increasing air CO_2 and seawater temperature would level up the DIC concentration by 122.1±20.0 μmol kg^{-1}, and pH and Ω_{arag} would be down to 7.78±0.01 and 2.12±0.22, respectively. Furthermore, the influence of submarine groundwater discharge and organic matter remineralization could reduce pH and Ω_{arag} to 7.56 ±0.01 (range=7.54–7.58) and 1.39±0.18 (range=1.00–1.65). The predicted Ω_{arag} values in bottom waters at some stations could be ~1.00, suggesting a high risk of seawater acidification in this coastal ecosystem at the end of this century.

In this coastal area, freshwater discharge from rivers is characterized by low DIC and TA, and therefore low carbonate ion concentrations and low Ω_{arag}. Thus, the dilution of freshwater in the plume area may result in additional acidification (Chou et al., 2013; Zhai et al., 2015). Furthermore, the anticipated increase of nutrient and organic carbon loading would inevitably enhance the coastal water acidification (Wang et al., 2014). In the context of global climate change, all these processes/factors would make ocean acidification in coastal areas a much more dynamic and severe phenomenon, whose controlling mechanisms require future consideration.

5. Conclusions

The present study reports for the first time the joint influence of coastal upwelling, submarine groundwater discharge and river plumes on carbonate dynamics in the NWSCS. While the coastal plume water featuring low seawater pCO_2, and high pH and Ω_{arag} was evident during both cruises, the present study revealed the year-to-year dynamic of the Pearl River Plume associated with the variability of river discharge and coastal currents. Upwelling was observed during both cruises but at different locations under different wind stress, coastal currents, and the influence of freshwater. The influence of submarine groundwater discharge also showed year-to-year difference, regulated by the varying precipitation rates. Coastal acidification is a complex phenomenon driven by multiple physical and biogeochemical processes. Our first

https://engine.scichina.com/doi/10.1007/s11430-021-9963-8

order predictions suggested that the increasing atmospheric CO_2 and seawater temperature would pose a high risk of seawater acidification in this coastal ecosystem at the end of this century, which could be amplified under the stress of river plume effects, and influence of submarine groundwater discharge and organic matter remineralization.

Acknowledgements *We thank Drs. Weidong ZHAI and Pinghe CAI who led the cruises as chief scientists, and Nan ZHENG, Yan YANG, Junqi ZHANG, Qian LI, Xu DONG, Yuancheng SU, Di QI and Bo YANG for their help in data collection. Jia ZHU and Zhenyu SUN assisted with CTD data collection and processing. We are grateful to the crews of the R/V Dongfanghong II for their help during the cruises. The authors declare that the study was conducted in the absence of any commercial or financial relationships that could be construed as a potential conflict of interest. This study was funded by the National Natural Science Foundation of China (Grant Nos. 42188102, 41206061) and the Hong Kong Research Grants Council (Grant No. T21-602/16-R).*

References

Barth J A, Menge B A, Lubchenco J, Chan F, Bane J M, Kirincich A R, McManus M A, Nielsen K J, Pierce S D, Washburn L. 2007. Delayed upwelling alters nearshore coastal ocean ecosystems in the northern California current. Proc Natl Acad Sci USA, 104: 3719–3724

Benson B B, Krause D J. 1984. The concentration and isotopic fractionation of oxygen dissolved in freshwater and seawater in equilibrium with the atmosphere1. Limnol Oceanogr, 29: 620–632

Borges A V, Frankignoulle M. 2002. Distribution of surface carbon dioxide and air-sea exchange in the upwelling system off the Galician coast. Glob Biogeochem Cycle, 16: 13-1–13-13

Cai W J, Dai M, Wang Y, Zhai W, Huang T, Chen S, Zhang F, Chen Z, Wang Z. 2004. The biogeochemistry of inorganic carbon and nutrients in the Pearl River estuary and the adjacent Northern South China Sea. Cont Shelf Res, 24: 1301–1319

Cai W J. 2011. Estuarine and coastal ocean carbon paradox: CO_2 sinks or sites of terrestrial carbon incineration? Annu Rev Mar Sci, 3: 123–145

Cao Z, Dai M, Zheng N, Wang D, Li Q, Zhai W, Meng F, Gan J. 2011. Dynamics of the carbonate system in a large continental shelf system under the influence of both a river plume and coastal upwelling. J Geophys Res, 116: G02010

Cao Z, Dai M, Evans W, Gan J, Feely R. 2014. Diagnosing CO_2 fluxes in the upwelling system off the Oregon-California coast. Biogeosciences, 11: 6341–6354

Carpenter J H. 1965. The Chesapeake Bay Institute technique for the Winkler dissolved oxygen method. Limnol Oceanogr, 10: 141–143

Chen Z, Gong W, Cai H, Chen Y, Zhang H. 2017. Dispersal of the Pearl River plume over continental shelf in summer. Estuar Coast Shelf Sci, 194: 252–262

Chou W C, Gong G C, Hung C C, Wu Y H. 2013. Carbonate mineral saturation states in the East China Sea: Present conditions and future scenarios. Biogeosciences, 10: 6453–6467

Dai G Y, Wang G Z, Li Q, Tan E H, Dai M H. 2021. Submarine groundwater discharge on the western shelf of the northern South China Sea influenced by the Pearl River plume and upwelling. J Geophys Res-Oceans, 126: e16859

Dai M H, Cao Z M, Guo X H, Zhai W D, Liu Z Q, Yin Z Q, Du C J. 2013. Why are some marginal seas sources of atmospheric CO_2? Geophys Res Lett, 40: 2154–2158

Dai M H, Gan J P, Han A Q, Kung H S, Yin Z. 2014. Physical dynamics and biogeochemistry of the Pearl River plume. In: Bianchi T, Allison M, Cai W J, eds. Biogeochemical Dynamics at Major River Coastal Interfaces. Cambridge: Cambridge University Press. 325–335

Dickson A G, Millero F J. 1987. A comparison of the equilibrium constants for the dissociation of carbonic acid in seawater media. Deep Sea Res Part A Oceanographic Res Papers, 34: 1733–1743

Dickson A G. 1990. Standard potential of the reaction: $AgCl(s)+12H_2(g)=Ag(s)+HCl(aq)$, and and the standard acidity constant of the ion HSO_4^- in synthetic sea water from 273.15 to 318.15 K. J Chem Thermodyn, 22: 113–127

Dong L, Su J, Ah Wong L, Cao Z, Chen J C. 2004. Seasonal variation and dynamics of the Pearl River plume. Cont Shelf Res, 24: 1761–1777

Dong X, Huang H, Zheng N, Pan A, Wang S, Huo C, Zhou K, Lin H, Ji W. 2017. Acidification mediated by a river plume and coastal upwelling on a fringing reef at the east coast of Hainan Island, Northern South China Sea. J Geophys Res-Oceans, 122: 7521–7536

Du C, Liu Z, Dai M, Kao S J, Cao Z, Zhang Y, Huang T, Wang L, Li Y. 2013. Impact of the Kuroshio intrusion on the nutrient inventory in the upper northern South China Sea: Insights from an isopycnal mixing model. Biogeosciences, 10: 6419–6432

Evans W, Hales B, Strutton P G, Ianson D. 2012. Sea-air CO_2 fluxes in the western Canadian coastal ocean. Prog Oceanogr, 101: 78–91

Feely R A, Sabine C L, Hernandez-Ayon J M, Ianson D, Hales B. 2008. Evidence for upwelling of corrosive "acidified" water onto the continental shelf. Science, 320: 1490–1492

Feely R A, Sabine C L, Byrne R H, Millero F J, Dickson A G, Wanninkhof R, Murata A, Miller L A, Greeley D. 2012. Decadal changes in the aragonite and calcite saturation state of the Pacific Ocean. Glob Biogeochem Cycle, 26: GB3001

Fong D A, Geyer W R. 2001. Response of a river plume during an upwelling favorable wind event. J Geophys Res, 106: 1067–1084

Friederich G E, Walz P M, Burczynski M G, Chavez F P. 2002. Inorganic carbon in the central California upwelling system during the 1997–1999 El Niño-La Niña event. Prog Oceanogr, 54: 185–203

Gan J P, Li L, Wang D X, Guo X G. 2009. Interaction of a river plume with coastal upwelling in the northeastern South China Sea. Cont Shelf Res, 29: 728–740

Gan J P, Lu Z M, Dai M H, Cheung A Y Y, Liu H B, Harrison P. 2010. Biological response to intensified upwelling and to a river plume in the northeastern South China Sea: A modeling study. J Geophys Res, 115: C09001

Gu H, Moore W S, Zhang L, Du J, Zhang J. 2012. Using radium isotopes to estimate the residence time and the contribution of submarine groundwater discharge (SGD) in the Changjiang effluent plume, East China Sea. Cont Shelf Res, 35: 95–107

Guo X H, Wong G T F. 2015. Carbonate chemistry in the Northern South China Sea Shelf-sea in June 2010. Deep Sea Res Part II, 117: 193–130

Guo X, Cai W J, Zhai W, Dai M, Wang Y, Chen B. 2008. Seasonal variations in the inorganic carbon system in the Pearl River (Zhujiang) estuary. Cont Shelf Res, 28: 1424–1434

Hales B, Takahashi T, Bandstra L. 2005. Atmospheric CO_2 uptake by a coastal upwelling system. Glob Biogeochem Cycle, 19: GB1009

Han A Q, Dai M H, Kao S J, Gan J P, Li Q, Wang L F, Zhai W D, Wang L. 2012. Nutrient dynamics and biological consumption in a large continental shelf system under the influence of both a river plume and coastal upwelling. Limnol Oceanogr, 57: 486–502

Hu J, Wang X H. 2016. Progress on upwelling studies in the China seas. Rev Geophys, 54: 653–673

Huang W J, Cai W J, Wang Y, Hu X, Chen B, Lohrenz S E, Chakraborty S, He R, Brandes J, Hopkinson C S. 2015. The response of inorganic carbon distributions and dynamics to upwelling-favorable winds on the northern Gulf of Mexico during summer. Cont Shelf Res, 111: 211–222

Jing Z, Qi Y, Du Y. 2011. Upwelling in the continental shelf of northern South China Sea associated with 1997–1998 El Niño. J Geophys Res, 116: C02033

Jing Z, Qi Y, Du Y, Zhang S, Xie L. 2015. Summer upwelling and thermal fronts in the northwestern South China Sea: Observational analysis of two mesoscale mapping surveys. J Geophys Res-Oceans, 120: 1993–2006

Labasque T, Chaumery C, Aminot A, Kergoat G. 2004. Spectrophotometric Winkler determination of dissolved oxygen: Re-examination of critical

https://engine.scichina.com/doi/10.1007/s11430-021-9963-8

factors and reliability. Mar Chem, 88: 53–60
Li Q, Guo X, Zhai W, Xu Y, Dai M. 2020. Partial pressure of CO_2 and air-sea CO_2 fluxes in the South China Sea: Synthesis of an 18-year dataset. Prog Oceanogr, 182: 102272
Lin P, Cheng P, Gan J, Hu J. 2016a. Dynamics of wind-driven upwelling off the northeastern coast of Hainan Island. J Geophys Res-Oceans, 121: 1160–1173
Lin P, Hu J, Zheng Q, Sun Z, Zhu J. 2016b. Observation of summertime upwelling off the eastern and northeastern coasts of Hainan Island, China. Ocean Dyn, 66: 387–399
Liu Q, Dai M H, Chen W F, Huh C A, Wang G, Li Q, Charette M A. 2012. How significant is submarine groundwater discharge and its associated dissolved inorganic carbon in a river-dominated shelf system? Biogeosciences, 9: 1777–1795
Liu Q, Charette M A, Henderson P B, McCorkle D C, Martin W, Dai M. 2014. Effect of submarine groundwater discharge on the coastal ocean inorganic carbon cycle. Limnol Oceanogr, 59: 1529–1554
Lui H K, Chen C T A, Lee J, Wang S L, Gong G C, Bai Y, He X. 2015. Acidifying intermediate water accelerates the acidification of seawater on shelves: An example of the East China Sea. Cont Shelf Res, 111: 223–233
Luo X, Jiao J J, Liu Y, Zhang X, Liang W, Tang D. 2017. Evaluation of water residence time, submarine groundwater discharge, and maximum new production supported by groundwater borne nutrients in a coastal upwelling shelf system. J Geophys Res-Oceans, 123: 631–655
Lü X G, Qiao F L, Wang G S, Xia C S, Yuan Y L. 2008. Upwelling off the west coast of Hainan Island in summer: Its detection and mechanisms. Geophys Res Lett, 35: L02604
McNeil B I, Matear R J. 2007. Climate change feedbacks on future oceanic acidification. Tellus B, 59: 191–198
Mehrbach C, Culberson C H, Hawley J E, Pytkowicx R M. 1973. Measurement of the apparent dissociation constants of carbonic acid in seawater at atmospheric pressure. Limnol Oceanogr, 18: 897–907
Meng F, Dai M, Cao Z, Wu K, Zhao X, Li X, Chen J, Gan J. 2017. Seasonal dynamics of dissolved organic carbon under complex circulation schemes on a large continental shelf: The northern South China Sea. J Geophys Res-Oceans, 122: 9415–9428
Ou S, Zhang H, Wang D. 2009. Dynamics of the buoyant plume off the Pearl River Estuary in summer. Environ Fluid Mech, 9: 471–492
Pierrot D, Lewis E, Wallace D W R. 2006. MS Excel program developed for CO_2 system calculations. Carbon Dioxide Information Analysis Center, Oak Ridge National Laboratory. Oak Ridge: U.S. Department of Energy
Redfield A C, Ketchum B H, Richards F A. 1963. The influence of organisms on the composition of seawater. In: Hill M N, ed. The Sea. New York: Wiley. 26–77
Risien C M, Reason C J C, Shillington F A, Chelton D B. 2004. Variability in satellite winds over the Benguela upwelling system during 1999–2000. J Geophys Res, 109: C03010
Santana-Casiano J M, González-Dávila M, Ucha I R. 2009. Carbon dioxide fluxes in the Benguela upwelling system during winter and spring: A comparison between 2005 and 2006. Deep-Sea Res Part II-Top Stud Oceanogr, 56: 533–541
Su J, Dai M, He B, Wang L, Gan J, Guo X, Zhao H, Yu F. 2017. Tracing the origin of the oxygen-consuming organic matter in the hypoxic zone in a large eutrophic estuary: The lower reach of the Pearl River Estuary, China. Biogeosciences, 14: 4085–4099
Sunda W G, Cai W J. 2012. Eutrophication induced CO_2-acidification of subsurface coastal waters: Interactive effects of temperature, salinity, and atmospheric PCO_2. Environ Sci Technol, 46: 10651–10659
Takahashi T, Olafsson J, Goddard J G, Chipman D W, Sutherland S C. 1993. Seasonal variation of CO_2 and nutrients in the high-latitude surface oceans: A comparative study. Glob Biogeochem Cycle, 7: 843–878
Tan E, Wang G, Moore W S, Li Q, Dai M. 2018. Shelf-scale submarine groundwater discharge in the northern South China Sea and East China Sea and its geochemical impacts. J Geophys Res-Oceans, 123: 2997–3013
Torres R. 2003. Continued CO_2 outgassing in an upwelling area off northern Chile during the development phase of El Niño 1997–1998 (July 1997). J Geophys Res, 108: 3336
Uppstrom L. 1967. Analysis of boron in seawater by a modified curcumin method. In: Martin D F, ed. Marine Chemistry, Vol. 1 (Analytical Methods), 2nd ed. New York: Marcei. Dekker. Inc. 1972, 389
Wang G, Jing W, Wang S, Xu Y, Wang Z, Zhang Z, Li Q, Dai M. 2014. Coastal acidification induced by tidal-driven submarine groundwater discharge in a coastal coral reef system. Environ Sci Technol, 48: 13069–13075
Wu K, Dai M, Li X, Meng F, Chen J, Lin J. 2017. Dynamics and production of dissolved organic carbon in a large continental shelf system under the influence of both river plume and coastal upwelling. Limnol Oceanogr, 62: 973–988
Xie L, Pallàs-Sanz E, Zheng Q, Zhang S, Zong X, Yi X, Li M. 2017. Diagnosis of 3D Vertical circulation in the upwelling and frontal zones east of Hainan Island, China. J Phys Oceanogr, 47: 755–774
Xu C, Xu Y, Hu J, Li S, Wang B. 2019. A numerical analysis of the summertime Pearl River plume from 1999 to 2010: Dispersal patterns and intraseasonal variability. J Mar Syst, 192: 15–27
Xu X M, Zang K P, Zhao H D, Zheng N, Hu C, Wang J Y. 2016. Monthly CO_2 at A4HDYD station in a productive shallow marginal sea (Yellow Sea) with a seasonal thermocline: Controlling processes. J Mar Syst, 159: 89–99
Xue L, Cai W J, Sutton A J, Sabine C. 2017. Sea surface aragonite saturation state variations and control mechanisms at the Gray's Reef time-series site off Georgia, USA (2006–2007). Mar Chem, 195: 27–40
Xue L, Wang H, Jiang L Q, Cai W J, Wei Q, Song H, Kuswardani R T D, Pranowo W S, Beck B, Liu L, Yu W. 2016. Aragonite saturation state in a monsoonal upwelling system off Java, Indonesia. J Mar Syst, 153: 10–17
Yang W, Guo X, Cao Z, Xu Y, Wang L, Guo L, Huang T, Li Y, Xu Y, Gan J, Dai M. 2021. Seasonal dynamics of the carbonate system under complex circulation schemes on a large continental shelf: The northern South China Sea. Prog Oceanogr, 197: 102630
Zhai W, Dai M, Cai W J, Wang Y, Hong H. 2005b. Erratum to "The partial pressure of carbon dioxide and air-sea fluxes in the northern South China Sea in spring, summer and autumn" [Marine Chemistry 96 (2005) 87–97]. Mar Chem, 103: 209–2007
Zhai W D, Dai M H, Chen B S, Guo X H, Li Q, Shang S L, Zhang C Y, Cai W J, Wang D X. 2013. Seasonal variations of sea-air CO_2 fluxes in the largest tropical marginal sea (South China Sea) based on multiple-year underway measurements. Biogeosciences, 10: 7775–7791
Zhai W, Dai M, Cai W J, Wang Y, Wang Z. 2005a. High partial pressure of CO_2 and its maintaining mechanism in a subtropical estuary: The Pearl River estuary, China. Mar Chem, 93: 21–32
Zhai W D, Zang K P, Huo C, Zheng N, Xu X M. 2015. Occurrence of aragonite corrosive water in the North Yellow Sea, near the Yalu River estuary, during a summer flood. Estuar Coast Shelf Sci, 166: 199–208
Zhang F, Zhang W, Yang Q. 2003. Characteristics of grain size distributions of surface sediments in the eastern South China Sea (in Chinese). Acta Sedimentol Sin, 21: 452–460
Zhao Y, Uthaipan K, Lu Z, Li Y, Liu J, Liu H, Gan J, Meng F, Dai M. 2021. Destruction and reinstatement of coastal hypoxia in the South China Sea off the Pearl River estuary. Biogeosciences, 18: 2755–2775
Zu T, Wang D, Gan J, Guan W. 2014. On the role of wind and tide in generating variability of Pearl River plume during summer in a coupled wide estuary and shelf system. J Mar Syst, 136: 65–79

(Responsible editor: Zhimin JIAN)

https://engine.scichina.com/doi/10.1007/s11430-021-9963-8